



Excavated carbon with embedded Si nanoparticles for ultrafast lithium storage



Geon-Hyoung An^a, Hyeonjin Kim^b, Hyo-Jin Ahn^{a,b,*}

^a Program of Materials Science and Engineering, Convergence Institute of Biomedical Engineering and Biomaterials, Seoul 139-743, Republic of Korea

^b Department of Materials Science and Engineering, Seoul National University of Science and Technology, Seoul 139-743, Republic of Korea

ARTICLE INFO

Article history:

Received 24 March 2018

Received in revised form 28 June 2018

Accepted 26 July 2018

Available online 2 August 2018

Keywords:

Li-ion battery

Excavated carbon

Mesoporous structure

Silicon

Ultrafast

ABSTRACT

Due to their excellent mechanical durability and high electrical conductivity, carbon and silicon composites are potentially suitable anode materials for Li-ion batteries with high capacity and long lifespan. Nevertheless, the limitations of the composites include their poor ionic diffusion at high current densities during cycling, which leads to low ultrafast performance. In the present study, seeking to improve the ionic diffusion using hydrothermal method, electrospinning, and carbonization, we demonstrate the unique design of excavated carbon and silicon composites (EC/Si). The outstanding energy storage performance of EC/Si electrode provides a discharge specific capacity, impressive rate performance, and ultrafast cycling stability.

© 2018 The Korean Society of Industrial and Engineering Chemistry. Published by Elsevier B.V. All rights reserved.

Introduction

Further advances in the field of portable electronics largely depends on the development of Li ion batteries (LIBs) characterized by high energy density, long lifespan, lower memory loss, and environmental friendliness [1–3]. However, due to the long charging time, LIBs do not demonstrated performance sufficient for their use in electric vehicles and robotics [4–6]. For instance, the LIBs of Tesla Model 3 need a long charging time (20–30 h at home or 5–6 h at a home charging point) [5,6]. In view of these restrictions, to meet the requirements for fully electric vehicles, an ideal LIB with high capacity and excellent ultrafast performance should be at least one order higher than the currently available LIBs. Therefore, the diverse approaches have been applied to achieve the high capacity and excellent ultrafast performance LIBs (called ultrafast LIBs) by the improvement of electrode materials, the interface management between the electrode materials and current collector, and the development of electrolyte [7–9]. Among these strategies, the ultrafast LIB performance is almost entirely decided by anode materials using electrochemical reactions with Li ions [7–9].

Among the anode materials, silicon (Si) with low working voltage and high theoretical capacity ($\sim 4200 \text{ mA h g}^{-1}$) has been

mainly recollected for the anode. However, as is well known, the significant challenge of Si is the structural deterioration from the large volume expansion of $\sim 300\%$, which results in an electrical connection loss [5,10–13]. Therefore, due to their excellent mechanical durability and high electrical conductivity, leading to high capacity and notable cycling stability, the carbon and silicon composites as anode materials are promising candidates for ultrafast LIBs [10–13]. Nevertheless, the carbon and silicon composites have a high barrier with the low ultrafast performance that results from a long ionic diffusion way at high current densities during cycling [10–13]. It is found that the ultrafast performance of LIBs is significantly decreased when the ionic and electronic transport properties are not optimized within the anode materials [14–16]. Therefore, the improved ionic and electronic behavior of carbon and silicon composites also needs to be deliberated by the advanced material structure.

In the present paper, we suggest a unique design of excavated carbon and silicon composites (EC/Si) that have the critical advantages of having an excavated structure with craters to guarantee ultrafast performance and mesopores for excellent cycling stability. EC/Si was fabricated by electrospinning and the carbonization process. In addition, the excavated structure was developed using the dissolution process of 10 wt.% zinc oxide (ZnO) nanoparticles during carbonization. In order to investigate the detailed structure effect, carbon and silicon composites (C/Si) without the usage of the ZnO nanoparticles and the mesoporous carbon and silicon composites (MC/Si) using 5 wt.% ZnO nanoparticles were also prepared.

* Corresponding author at: Department of Materials Science and Engineering, Seoul National University of Science and Technology, Seoul 139-743, South Korea.
E-mail address: hjahn@seoultech.ac.kr (H.-J. Ahn).

Results and discussion

As illustrated in Fig. 1, the unique architecture of EC/Si was synthesized via a dissolution process of ZnO nanoparticles by electrospinning and the carbonization process. For the electrospinning solution, PAN, the carbon-coated Si nanoparticle (C@Si), and ZnO particles were dispersed in *N,N*-Dimethylformamide by magnetic string for 5 h. In general, the Si nanoparticles are easy aggregated using the solution-based process and oxidized during the stabilization process of polymer before carbonization process, which leads to poor energy storage performance. Therefore, in this study, the carbon-coated Si nanoparticles and ZnO nanoparticles were combined in polyacrylonitrile (PAN) nanofibers (see Fig. 1a). At more than 419.5 °C during the carbonization process at 800 °C in nitrogen atmosphere, ZnO was reduced to Zn and then dissolved to reach thermodynamic stability, leading to the formation of mesoporous structure (see Fig. 1b). Of note, due to the partially oxidation–reduction reaction between the carbon and oxygen in ZnO (Fig. 1c), the craters formed onto the surface. Thus, the mesoporous structure was fabricated using the molten of ZnO. Finally, EC/Si (Fig. 1d) was successfully prepared by a removal of residual Zn using hydrochloric acid.

To improve the dispersion of the Si nanoparticles into the carbon matrix, the Si nanoparticle with the 23–51 nm was coated by carbon layer with the thickness of 7–10 nm (see Fig. S1 in Supporting information (SI)). Thus, by an effective use of the carbon matrix, we demonstrated that the well-dispersed Si nanoparticles into carbon matrix could provide an excellent cycling stability [5,10,12]. The morphological properties were proved using low-resolution (Fig. 2a–c) and high-resolution (Fig. 2d–f) micrographs of the C/Si, MC/Si, and EC/Si by scanning electron microscopy (SEM). All samples indicated the fibre networks with the diameter of 291–305 nm, which led to an excellent electron transfer during the charging and discharging. C/Si (Fig. 2a and d) and MC/Si (Fig. 2b and e) showed a flat surface without aggregated nanoparticles on the surface, signifying the embedded Si nanoparticles into the carbon matrix. Using an effective accommodation of volume expansion for the Si nanoparticles, the carbon matrix could improve the capacity and cycling stability [14–20]. On the other hand, EC/Si (Fig. 2c and f) presented a novel architecture of an excavated structure with craters (16–53 nm). The formation of craters at the edge surface of EC/Si can be attributed to the carbon decomposition that depends on the

partially oxidation–reduction reaction between the carbon and oxygen in ZnO during carbonization. The novel architecture with craters can effectively reduce a diffusion Li-ion pathway during the charging and discharging, leading to an outstanding ultrafast performance in lithium storage [5,7]. However, for an increased amount of the ZnO nanoparticles (see Fig. S2), nanoparticle structures are formed due to the excessive decomposition of carbon. Therefore, EC/Si was optimized using 15 wt.% ZnO nanoparticles in an electrospinning solution.

Transmission electron microscopy (TEM, Gwangju Center, Korea Basic Science Institute) was further performed to probe the nanostructure properties using low-resolution (Fig. 3a–c) and high-resolution (Fig. 3d–f) micrographs of C/Si, MC/Si, and EC/Si, respectively. As shown in Fig. S3, after electrospinning, the C@Si and ZnO nanoparticles were combined in the PAN nanofibers without any aggregation. The Si nanoparticles of C/Si (Fig. 3a and d) were completely embedded into the carbon matrix. MC/Si (Fig. 3b and e) showed mesopores and embedded Si nanoparticles (the dark region) in the carbon matrix. Interestingly, EC/Si (Fig. 3c and f) showed a distinct excavated structure composed of mesopores and craters generated by the dissolution process of the ZnO particles during carbonization. Thus, the ZnO nanoparticles are promising candidates for the formation of mesopores and craters during carbonization. In addition, to investigate the localized structural information of carbon and Si nanoparticles, selected-area electron diffraction (SAED) pattern was performed, as shown in Fig. S4 [20]. The carbon spots of all samples exhibited the broad diffuse ring patterns, implying the amorphous structure. On the other hand, the Si spots displayed the sharp diffuse ring patterns, signifying a polycrystalline characteristic structure.

Fig. 4a shows the X-ray diffractometry (XRD) pattern of C/Si, MC/Si, and EC/Si conducted to inspect the crystal features. All architectures showed broad peaks around 25°, which corresponds to the (002) plane of graphite [21–23]. For comparison, the diffraction pattern of pure Si is displayed. The main reflections of Si were observed at 28.5°, 47.4°, and 56.3°, corresponding to the (111), (220), and (311) planes with the face-centred structure [5,10,24]. Therefore, the XRD results indicate that the generation process of the mesoporous structure during carbonization was not a crystallinity transformation of Si. To further inspect the chemical bonding states, X-ray photoelectron spectroscopy (XPS) was performed. C 1s signals (Fig. 4b) of EC/Si were divided into four peaks at 284.5, 286.3, 287.3, and 288.9 eV in connection with C–C

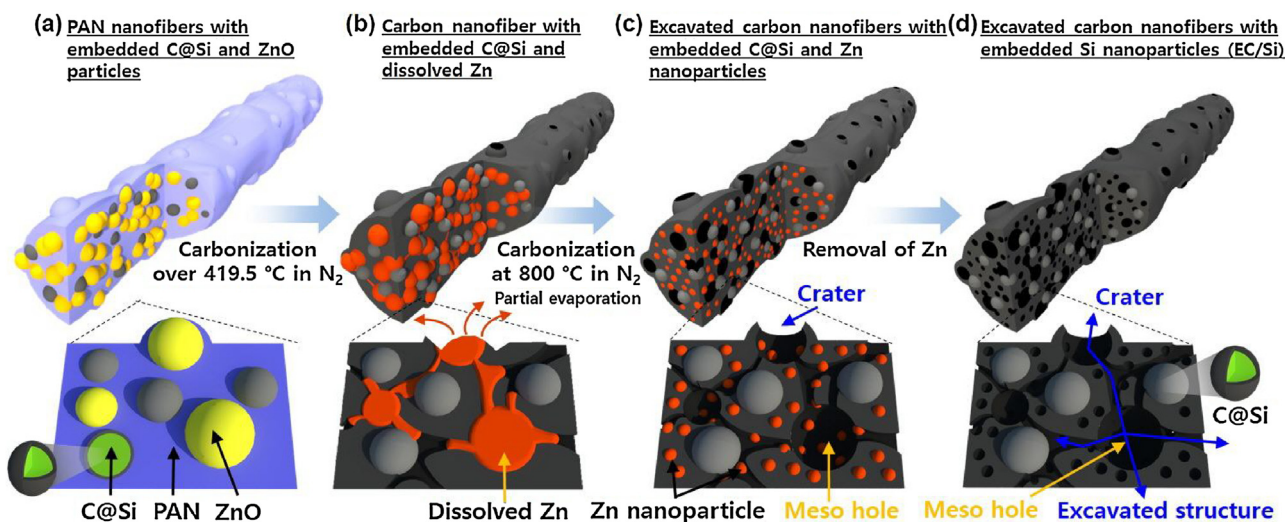


Fig. 1. Schematic representation of the fabrication procedures for (a) PAN nanofibers with embedded C@Si and ZnO particles; (b) carbon nanofiber with embedded C@Si and dissolved Zn; (c) excavated carbon nanofibers with embedded C@Si and Zn nanoparticles; and (d) excavated carbon nanofibers with embedded Si (EC/Si).

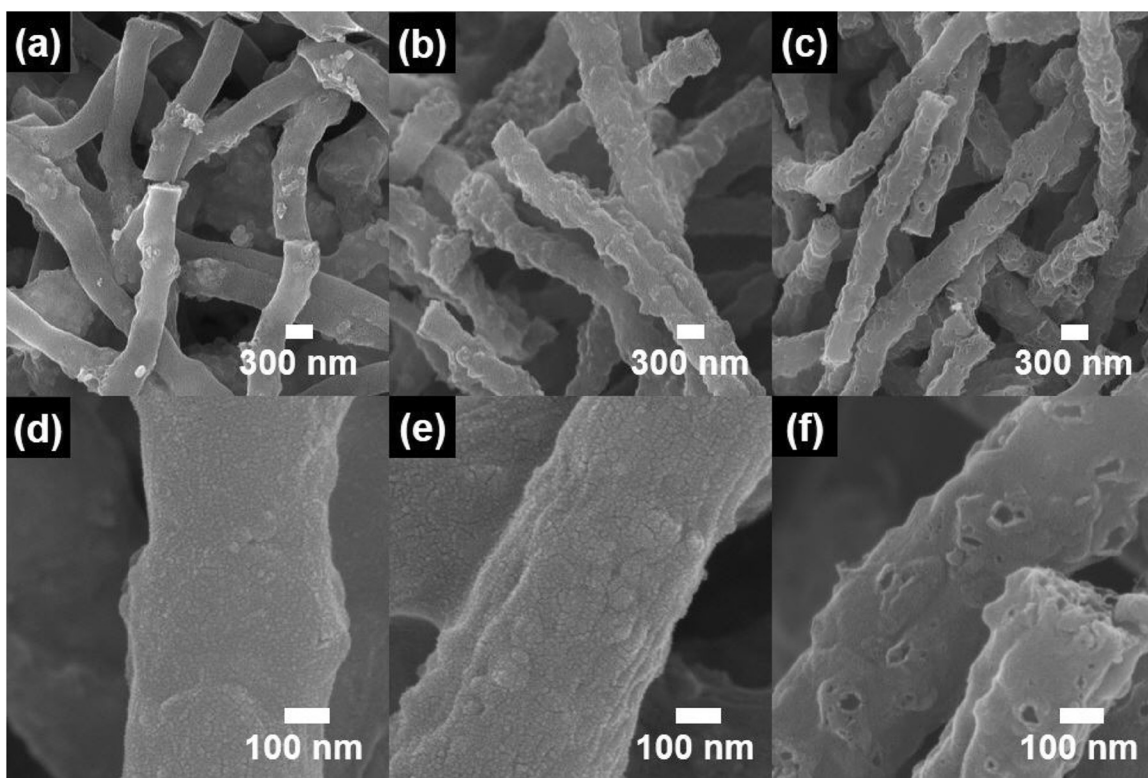


Fig. 2. (a–c) Low-resolution and (d–f) high-resolution SEM images of C/Si, MC/Si, and EC/Si.

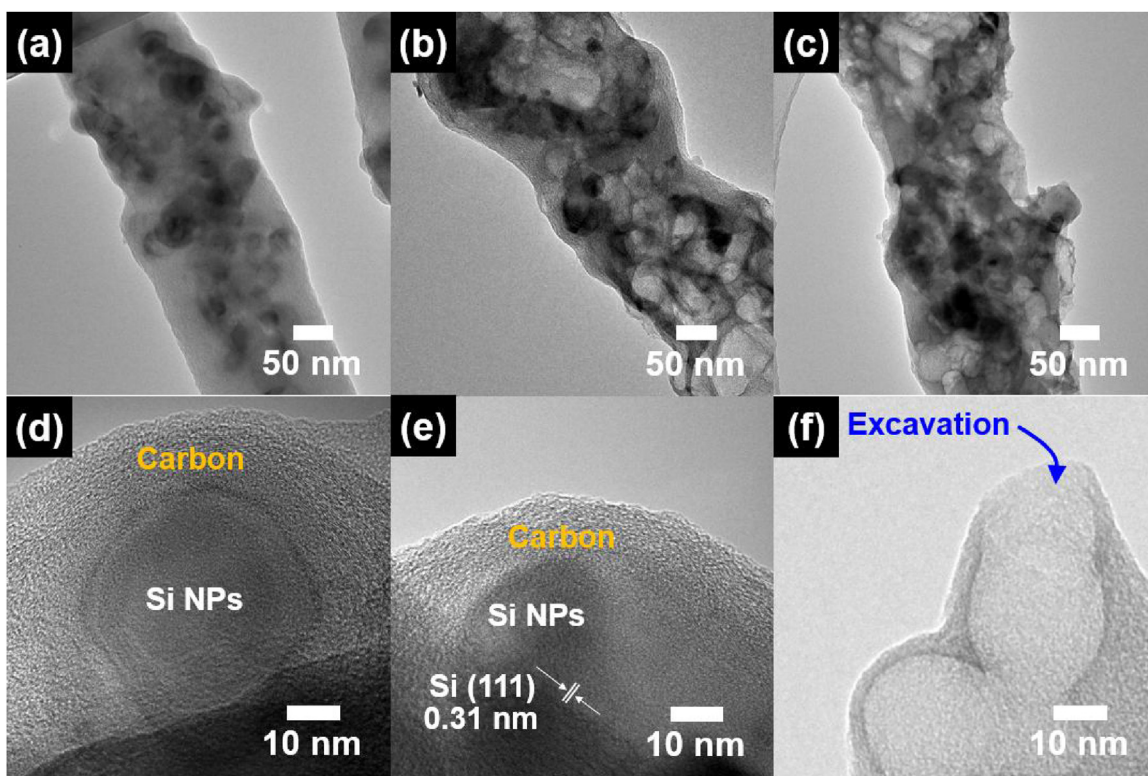


Fig. 3. (a–c) Low-resolution and (d–f) high-resolution TEM images of C/Si, MC/Si, and EC/Si.

groups, C—O groups, C=O groups, and O—C=O groups, respectively [25,26]. The chemical bonding on the surface of carbon and Si composites is crucial owing to the Si oxide with low electrical conductivity, leading to poor electrochemical performance. Si—2p

signals (Fig. 4c) of EC/Si monitored one signals at 99.6 eV, which corresponds to Si (0), indicating that the carbon layer on the Si nanoparticles could efficiently prevent the oxidation of Si and a well-dispersed nanostructure in carbon matrix during

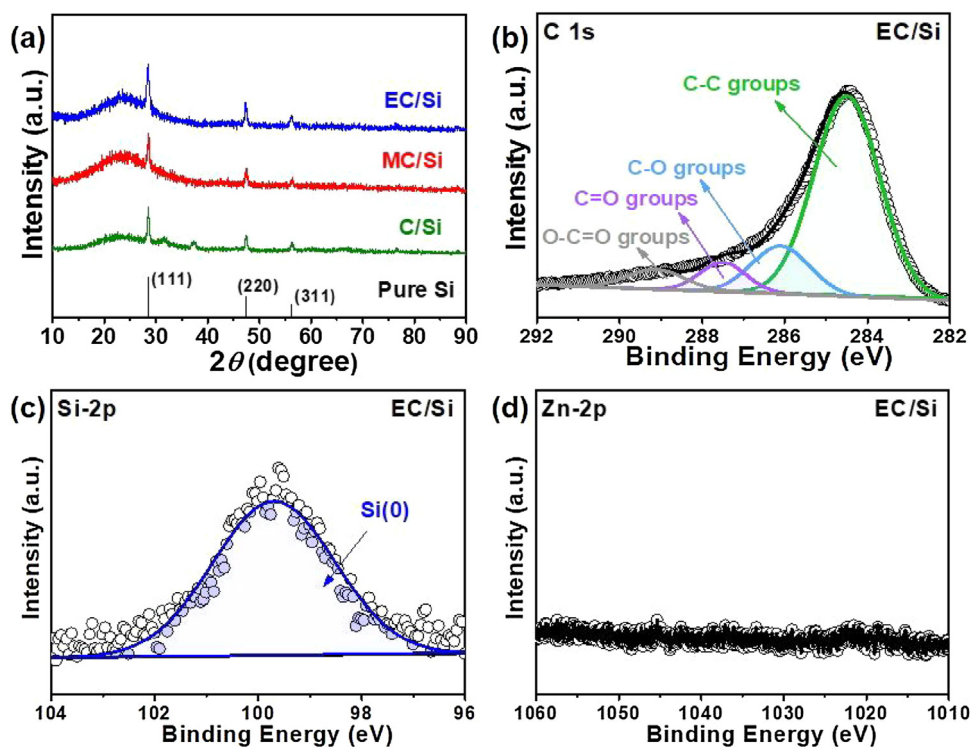


Fig. 4. (a) The XRD patterns of C/Si, MC/Si, and EC/Si; XPS spectra of (b) C 1s, (c) Si 2p, and (d) Zn 2p of EC/Si.

carbonization [5]. Zn 2p signals (Fig. 4d) of EC/Si are not visible, meaning that the residual Zn after carbonization was completely removed by hydrochloric acid. In addition, C/Si, MC/Si, and EC/Si demonstrated the existence of the Si nanoparticles in the carbon matrix by the thermogravimetric analysis (see Fig. S5) using the weight losses of 62, 55, and 53%.

In order to inspect the porous structure of C/Si, MC/Si, and EC/Si, N_2 adsorption/desorption isotherms were performed by the BET analysis (Fig. 5a). According to the International Union of Pure and Applied Chemistry [18,27], the pore structure can be classified by micropore (pore width, <2 nm) and mesopore (pore width, 2–50 nm). The isotherms of C/Si and MC/Si reveal Type I characteristics, meaning the micropores. In general, the carbon and Si nanoparticle composites have been mostly studied for the volume expansion of Si and electrical conductivity of carbon [10–13]. However, the ultrafast LIBs should be considered to be essential for diffusion performance of the Li ions. Due to their small pore size, the micropores are not suitable for ultrafast ion diffusion. Therefore, ultrafast LIBs require the development of mesopores for carbon and Si nanoparticle composites as electrode materials. The isotherm of MC/Si, and EC/Si exhibit Type IV characteristics,

signifying the mesopores at high pressures ($P/P_0 > 0.4$). Specifically, EC/Si shows the distinct interval of isotherm, meaning that the excavated structure with craters was composed of a mesoporous structure. The specific surface area, average pore diameter, total pore volume, and pore volume fraction are summarized in Table S1. EC/Si shows a higher mesopore distribution of 52.6% than the previously studied values of carbon and Si nanoparticle composites as anode electrodes. Barrett–Joyner–Halenda (Fig. 5b) was measured to investigate the pore size distributions and pore volumes. Agreeably with the SEM and TEM consequences, EC/Si displays mesopore distribution from 15 to 45 nm. In addition, the average mesopore diameter of C/Si, MC/Si, and EC/Si is summarized in Table S2. Therefore, the development of the mesoporous structure of EC/Si is essential for a shorter diffusion way during the ultrafast performance.

Electrochemical characterizations were analysed using the CR-2032 coin cells (half-type) with the Li metal as the counter electrode in a glove box. In addition, the C@Si was prepared for comparison. Electrochemical impedance spectroscopy (EIS) was performed using fresh cells to evaluate the effect of the excavated structure on the energy storage performance in anodes. Fig. 6a

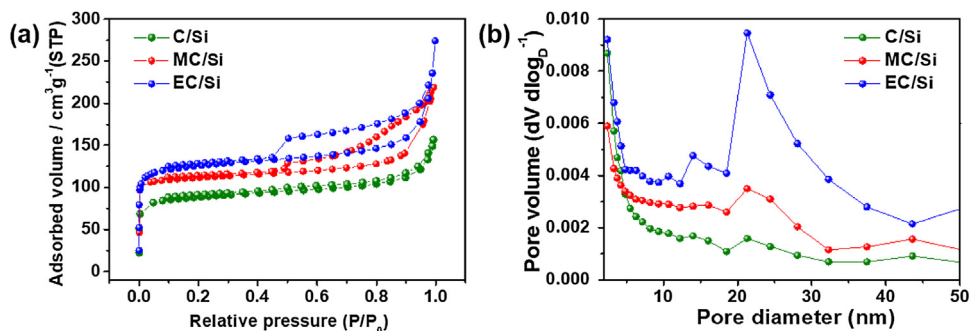


Fig. 5. (a) N_2 adsorption/desorption isotherms and (b) BJH pore size distributions of C/Si, MC/Si, and EC/Si.

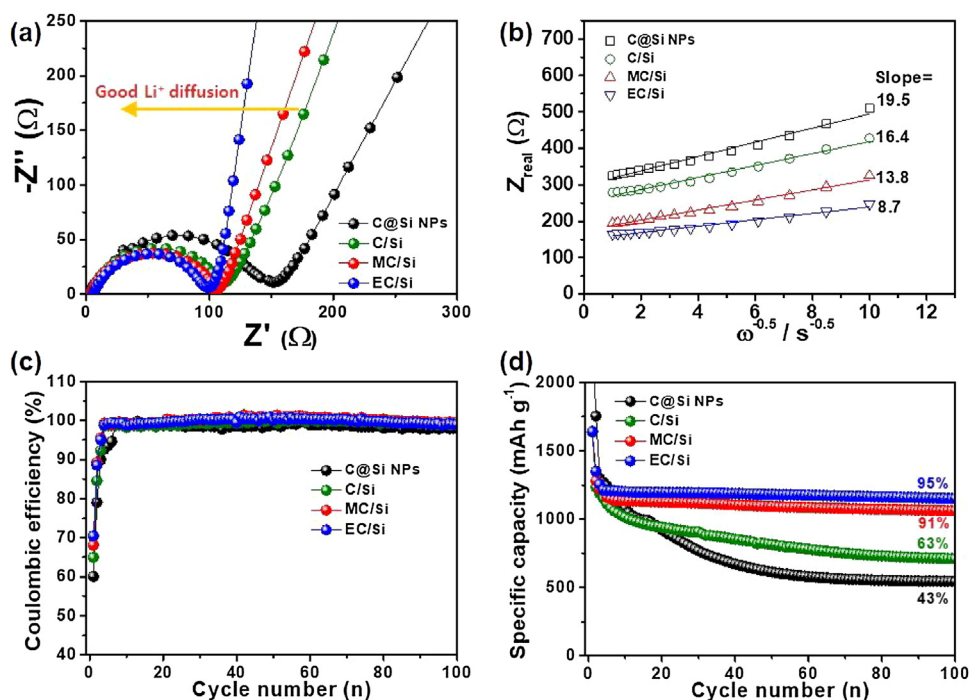


Fig. 6. (a) Nyquist plots in the frequency range of 10^5 – 10^{-2} Hz; (b) The relationship between Z_{real} and $\omega^{-1/2}$ in the low frequency range; (c) Coulombic efficiency; and (d) cycling stability of the C/Si, MC/Si, and EC/Si electrodes at current densities of 100 mA g^{-1} over 100 cycles.

shows Nyquist plots in the frequency range of 10^5 – 10^{-2} Hz. The semicircle in the medium-frequency region shows the charge transfer resistance (R_{ct}), and it can be observed that R_{ct} of EC/Si electrode is smaller than that of the C@Si NPs, C/Si, and MC/Si electrodes. The lowest values of R_{ct} indicates the faster reaction kinetics between the electrolyte and the electrode interface. In the low frequency region, the interfacial diffusion resistance of Li ions corresponds to Warburg impedance. The straight sloping line of EC/Si electrode means the lowest Warburg impedance related to a shorter Li-ion diffusion pathway as compared to the C/Si and MC/Si electrodes. Moreover, the Warburg impedance coefficients (σ_w) could be earned by the sloping line of Warburg impedance using Z_{real} and the square root of the frequency ($\omega^{-1/2}$) (see Eqs. (1) and (2)): [5,28]

$$Z_{\text{real}} = R_e + R_{\text{ct}} + \sigma_w \omega^{-1/2} \quad (1)$$

$$D = R^2 T^2 / 2 A^2 n^4 F^4 C^2 \sigma_w^2 \quad (2)$$

where D is the Li diffusion coefficient, R is the constant of gas, T is temperature, F is Faraday's constant, A is the electrode area, n is the number of electron/molecule, and C is a molar concentration of Li ions. Fig. 6b displays the relationship between Z_{real} and $\omega^{-1/2}$. σ_w of C@Si NPs, C/Si, MC/Si, and EC/Si electrodes amounted to 19.5, 16.4, 13.8, and $8.7 \Omega \text{ cm}^2 \text{ s}^{-1/2}$, respectively. In addition, the Li diffusion was calculated by σ_w . The Li diffusion value of C@Si NPs, C/Si, MC/Si, and EC/Si electrodes was 8.9×10^{-13} , 1.2×10^{-12} , 1.7×10^{-12} , and $4.4 \times 10^{-12} \text{ cm}^2 \text{ s}^{-1}$, respectively. These results provide evidence for an improved ionic diffusion performance based on the excavated structure of the EC/Si electrode. To characterize the electrochemical performances of electrodes, galvanostatic cycling tests were performed between 0.05 to 3.00 V at the current rate of 100 mA g^{-1} over 100 cycles (see Fig. 6c and d). The initial Coulombic efficiency (Fig. 6c) of the C@Si NPs, C/Si, MC/Si, and EC/Si electrodes was 60.0, 64.9, 68.0, and 70.4%, respectively. The initial irreversible capacities can be attributed to the formation of the solid-electrolyte

interphase (SEI) layers on the electrode surface due to the reductive disintegration of the electrolyte [29,30]. Nevertheless, the EC/Si electrode has a high initial Coulombic efficiency, implying the novel mesoporous structure with craters for favourable first cycling. Additionally, the charging and discharging curves of all electrodes revealed the typical electrochemical reactions of carbon and Si (see Fig. S6). After 100 cycles, the C@Si NPs electrode had a low discharge specific capacity of 543 mAh g^{-1} , which was mainly due to the large volume expansion of the Si nanoparticles during cycling. Therefore, the introduction of the carbon matrix is indispensable for the excellent cycling stability. The C/Si electrode showed a discharge specific capacity of 710 mAh g^{-1} with a relatively poor cycling retention of 61%. On the other hand, the MC/Si and EC/Si electrodes indicated the high discharge specific capacity of 1061 and 1151 Ah g^{-1} with outstanding cycling retentions of 91 and 95%, respectively. In addition, the EC/Si electrode had a higher discharge specific capacity after 100 cycles than the previously reported electrodes using carbon and Si composites (see Table S3 for a summary) [30–47]. The improved cycling retention can be ascribed to the mesoporous structure with mesopores, which leads to an expeditious accommodation of Si nanoparticles during cycling.

Owing to rapid expansion of application areas of LIBs, their rate and ultrafast performance have recently attracted considerable attention. The rate performance of the C@Si NPs, C/Si, MC/Si, and EC/Si electrodes was performed at current densities ranging from 100 to 2000 mA g^{-1} (see Fig. 7a). It is obvious that the discharge specific capacities of all electrodes reduce with the increase of current density due to the decreased time for the Li-ion diffusion. The C@Si NPs, C/Si, and MC/Si electrodes showed a poor rate performance, meaning that conventional design of electrode materials makes it difficult to receive fast ions at a high rate current density. Therefore, the excavated structure with craters of the EC/Si electrode has been devised to decrease a diffusion way. Of note, at different current densities ranging from 100 to 2000 mA g^{-1} , the EC/Si electrode showed the outstanding rate performance

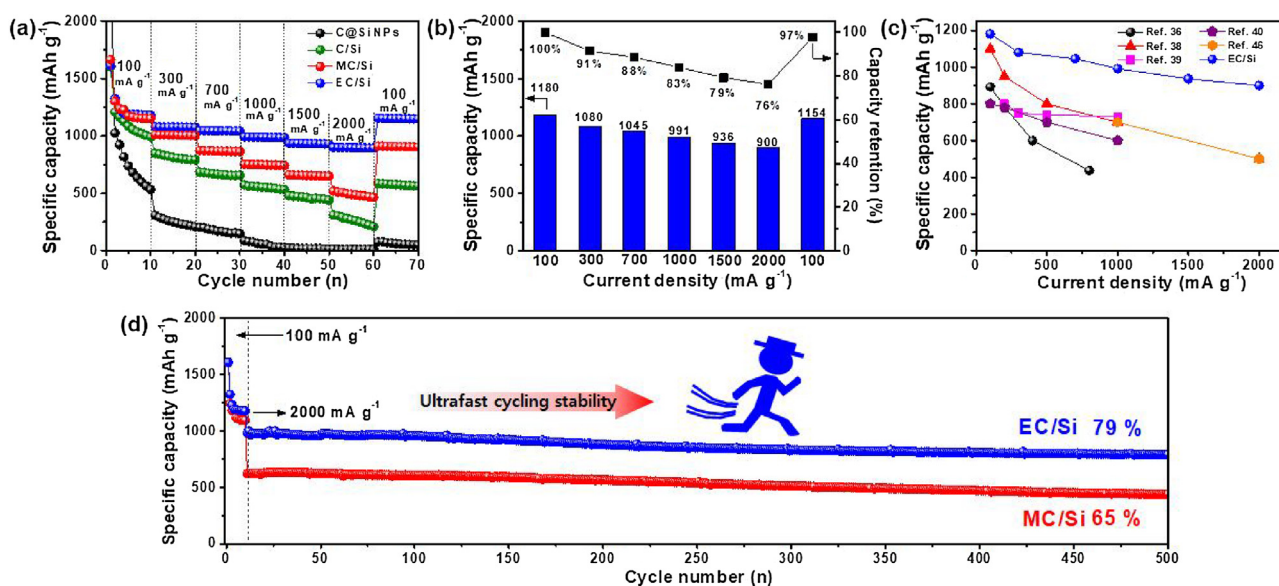


Fig. 7. (a) Rate performance at different current densities ranging from 100 to 2000 mA g⁻¹; (b) the detailed specific capacities and capacity retentions of the EC/Si electrode with increasing current densities; (c) comparison of high-rate performance with the previously reported electrodes using carbon and Si composites in LIBs; (d) ultrafast cycling stability at the current density of 2000 mA g⁻¹ over 500 cycles.

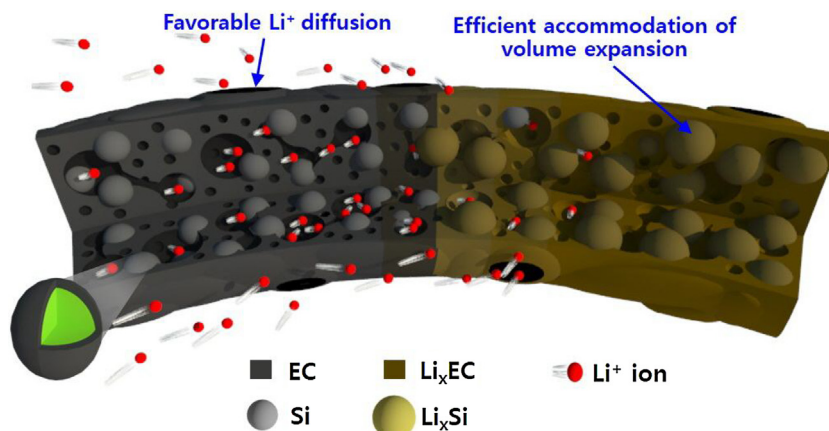


Fig. 8. The proposed design of the EC/Si electrode during the Li-ion insertion.

of 1180 to 894 mA h g⁻¹. Furthermore, the specific capacities and the capacity retentions at current densities from 100 to 2000 mA g⁻¹ of the EC/Si electrode are shown in Fig. 7b. After a rate test at high-rate densities, the EC/Si electrode presented the excellent capacity retention of 98% at 100 mA g⁻¹. The improved rate performance was the highest as compared to the previously reported electrodes using carbon and Si composites (see Fig. 7c) [36,38–40,46]. In addition, the ultrafast cycling stability is crucial for the use of LIBs in realistic applications. Fig. 7d shows the ultrafast cycling stability of the MC/Si and EC/Si electrodes at the high current density of 2000 mA g⁻¹. The EC/Si electrode exhibited a long-life cycling stability over 500 cycles with the discharge specific capacity of 790 mA h g⁻¹ without any structural changes from the initial structure (see Fig. S7). The enhanced rate and ultrafast cycling performance of EC/Si electrode is mainly due to the excavated structure with craters, leading to a short ionic diffusion way and a favourable ionic diffusion.

In sum, the impressive energy storage performance of the EC/Si electrode was attained due to establishing a novel structure (see Fig. 8). The mesoporous structure with mesopores enables the excellent cycling stability using the competent accommodation of

volume change of the Si nanoparticles at a low current density. In addition, the excavated structure with craters provides the short ionic diffusion way, which results in the ultrafast performance.

Conclusion

In the present study, EC/Si, which was prepared by the hydrothermal method, electrospinning, and carbonization, had a unique excavated structure consisting of mesopores (mesopore volume fraction of 52.6%) and craters (16–53 nm) as well as fibre networks. The outstanding energy storage performance of the EC/Si electrode, as evidenced by a discharge specific capacity (1151 mA h g⁻¹ after 100 cycles), impressive rate performance at 2000 mA g⁻¹ (894 mA h g⁻¹), and ultrafast cycling stability at 2000 mA g⁻¹ after 500 cycles (790 mA h g⁻¹), was obtained. The mesoporous structure was used to enhance the high discharge specific capacity with an excellent cycling stability. The excavated structure with craters also helps to improve the rate and ultrafast performance, enabling the improved ionic diffusion ability. Therefore, our approach offers a new strategy to not only fabricate the ultrafast lithium storage for fundamental research, but also to

improve an ionic diffusion performance for realistic use of LIBs in energy storage devices.

Acknowledgments

This work was supported by the Technology Innovation Program (10080656, Development of ceramic/carbon convergence and integration anode material for 10C fast charging Lithium ion battery) funded by the Ministry of Trade, Industry & Energy (MOTIE, Korea).

Appendix A. Supplementary data

Supplementary data associated with this article can be found in the online version, at <https://doi.org/10.1016/j.jiec.2018.07.039>

References

- [1] M. Armand, J.-M. Tarascon, *Nature* 451 (2008) 652.
- [2] P.G. Bruce, B. Scrosati, J.-M. Tarascon, *Angew. Chem. Int. Ed.* 47 (2008) 2930.
- [3] J.W. Choi, D. Aurbach, *Nat. Rev. Mater.* 1 (2016) 16013.
- [4] J.-H. Kim, M.-J. Jung, M.-J. Kim, Y.-S. Lee, *J. Ind. Eng. Chem.* 61 (2018) 368.
- [5] G.-H. An, H. Kim, H.-J. Ahn, *ACS Appl. Mater. Interfaces* 10 (2018) 6235.
- [6] S. Ko, C.W. Lee, J.S. Im, *J. Ind. Eng. Chem.* 36 (2016) 125.
- [7] G.-H. An, D.-Y. Lee, H.-J. Ahn, *ACS Appl. Mater. Interfaces* 9 (2017) 12478.
- [8] D.-S. Lee, Y.-H. Choi, H.-D. Jeong, *J. Ind. Eng. Chem.* 53 (2017) 82.
- [9] G.-H. An, D.-Y. Lee, Y.-J. Lee, H.-J. Ahn, *ACS Appl. Mater. Interfaces* 8 (2016) 30264.
- [10] G.-H. An, H.-J. Ahn, *J. Alloys Compd.* 710 (2017) 274.
- [11] M. Choi, W. William, J. Hwang, D. Yoon, J. Kim, *J. Ind. Eng. Chem.* 59 (2018) 160.
- [12] C. Kim, D. Verma, D.H. Nam, W. Chang, J. Kim, *J. Ind. Eng. Chem.* 52 (2017) 260.
- [13] H. Li, Z. Wang, L. Chen, X. Huang, *Adv. Mater.* 21 (2009) 4593.
- [14] Y. Tang, Y. Zhang, W. Li, B. Ma, X. Chen, *Chem. Soc. Rev.* 44 (2015) 5926.
- [15] S. Goriparti, E. Miele, F.D. Angelis, E.D. Fabrizio, R.P. Zaccaria, C. Capigli, *J. Power Sources* 257 (2014) 421.
- [16] N. Nitta, G. Yushin, *Part. Part. Syst. Char.* 31 (2014) 317.
- [17] B.-H. Kim, J.-H. Kim, J.-G. Kim, J.S. Im, C.W. Lee, S. Kim, *J. Ind. Eng. Chem.* 45 (2017) 99.
- [18] S.-J. Kim, M.-C. Kim, S.-B. Han, G.-H. Lee, H.-S. Choe, S.-H. Moon, D.-H. Kwak, S. Hong, K.-W. Park, *J. Ind. Eng. Chem.* 49 (2017) 105.
- [19] L. Hamenu, A. Madzvamuse, L. Mohammed, Y.M. Lee, J.M. Ko, C.Y. Bon, S.J. Kim, W.I. Cho, Y.G. Baek, J. Park, *J. Ind. Eng. Chem.* 53 (2017) 241.
- [20] B. Hou, D. Parker, G.P. Kissling, J.A. Jones, D. Cherns, D.J. Fernin, *J. Phys. Chem. C* 117 (2013) 6814.
- [21] G.-H. An, H.-J. Ahn, *Carbon* 65 (2013) 87.
- [22] G.-H. An, J.I. Sohn, H.-J. Ahn, *J. Mater. Chem. A* 4 (2016) 2049.
- [23] G.-H. An, H.-J. Ahn, W.-K. Hong, *J. Power Sources* 274 (2015) 536.
- [24] P.R. Ilango, R. Gnanamuthu, Y.N. Jo, C.W. Lee, *J. Ind. Eng. Chem.* 36 (2016) 121.
- [25] G.-H. An, D.-Y. Lee, H.-J. Ahn, *ACS Appl. Mater. Interfaces* 8 (2016) 19466.
- [26] G.-H. An, B.-R. Koo, H.-J. Ahn, *Phys. Chem. Chem. Phys.* 18 (2016) 6587.
- [27] Y.-W. Lee, D.-M. Kim, S.-J. Kim, M.-C. Kim, H.-S. Choe, K.-H. Lee, J.I. Sohn, S.N. Cha, J.M. Kim, K.-W. Park, *ACS Appl. Mater. Interfaces* 8 (2016) 7022.
- [28] Y. Yi, G.-H. Lee, J.-C. Kim, H.-W. Shim, D.-W. Kim, *Chem. Eng. J.* 327 (2017) 297.
- [29] G.-H. An, H.-J. Ahn, *J. Power Sources* 272 (2014) 828.
- [30] B.-S. Lee, S.-B. Son, K.-M. Park, J.-H. Seo, S.-H. Lee, I.-S. Choi, K.-H. Oh, W.-R. Yu, *J. Power Sources* 206 (2012) 267.
- [31] K. Fu, Y. Lu, M. Dirican, C. Chen, M. Yanilmaz, Q. Shi, P.D. Bradford, X. Zhang, *Nanoscale* 6 (2014) 7489.
- [32] N.T. Hieu, J. Suk, D.W. Kim, O.H. Chung, J.S. Park, Y. Kang, *Synth. Met.* 198 (2014) 36.
- [33] Y. Li, B. Guo, L. Ji, Z. Lin, G. Xu, Y. Liang, S. Zhang, O. Toprakci, Y. Hu, M. Alcoutlabi, X. Zhang, *Carbon* 51 (2013) 185.
- [34] L. Xue, K. Fu, Y. Li, G. Xu, Y. Lu, S. Zhang, O. Toprakci, X. Zhang, *Nano Energy* 2 (2013) 361.
- [35] L. Ji, X. Zhang, *Energy Environ. Sci.* 3 (2010) 124.
- [36] M. Dirican, O. Yildiz, Y. Lu, X. Fang, H. Jiang, H. Kizil, X. Zhang, *Electrochim. Acta* 169 (2015) 52.
- [37] Y. Li, Y. Sun, G. Xu, Y. Lu, S. Zhang, L. Xue, J.S. Jur, X. Zhang, *J. Mater. Chem. A* 2 (2014) 11417.
- [38] Y. Liu, K. Huang, Y. Fan, Q. Zhang, F. Sun, T. Gao, Z. Wang, J. Zhong, *Electrochim. Acta* 102 (2013) 246.
- [39] M.-S. Wang, W.-L. Song, J. Wang, L.-Z. Fan, *Carbon* 81 (2015) 337.
- [40] Z.-L. Xu, B. Zhang, J.-K. Kim, *Nano Energy* 6 (2014) 27.
- [41] X. Fan, L. Zou, Y.-P. Zheng, F.-Y. Kang, W.-C. Shen, *Electrochem. Solid State Lett.* 12 (2009) A199.
- [42] B.-S. Lee, S.-B. Son, J.-H. Seo, K.-M. Park, G. Lee, S.-H. Lee, K.H. Oh, J.-P. Ahn, W.-R. Yu, *Nanoscale* 5 (2013) 4790.
- [43] B.-S. Lee, H.-S. Yang, H. Jung, S.-Y. Jeon, C. Jung, S.-W. Kim, J. Bae, C.-L. Choong, J. Im, U.-I. Chung, J.-J. Park, W.-R. Yu, *Nanoscale* 6 (2014) 5989.
- [44] Y.-C. Zhang, Y. You, S. Xin, Y.-X. Yin, J. Zhang, P. Wang, X.-s. Zheng, F.-F. Cao, Y.-G. Guo, *Nano Energy* 25 (2016) 120.
- [45] J. Shin, K. Park, W.-H. Ryu, J.-W. Jung, Il-Doo Kim, *Nanoscale* 6 (2014) 12718.
- [46] Y. Chen, Y. Hu, J. Shao, Z. Shen, R. Chen, X. Zhang, X. He, Y. Song, X. Xing, *J. Power Sources* 298 (2015) 130.
- [47] J. Yang, Y.X. Wang, S.L. Chou, R. Zhang, Y. Xu, J. Fan, W.X. Zhang, H.K. Liu, D. Zhao, S.X. Dou, *Nano Energy* 18 (2015) 133.